nature geoscience

ARTICLES

https://doi.org/10.1038/s41561-019-0415-6

Optimal depth of subvolcanic magma chamber growth controlled by volatiles and crust rheology

Christian Huber[1]*, Meredith Townsend[1,2], Wim Degruyter[3] and Olivier Bachmann[4]

Storage pressures of magma chambers influence the style, frequency and magnitude of volcanic eruptions. Neutral buoyancy or rheological transitions are commonly assumed to control where magmas accumulate and form such chambers. However, the density of volatile-rich silicic magmas is typically lower than that of the surrounding crust, and the rheology of the crust alone does not define the depth of the brittle–ductile transition around a magma chamber. Yet, typical storage pressures inferred from geophysical inversions or petrological methods seem to cluster around 2 ± 0.5 kbar in all tectonic settings and crustal compositions. Here, we use thermomechanical modelling to show that storage pressure is controlled by volatile exsolution and crustal rheology. At pressures ≲1.5 kbar, and for geologically realistic water contents, chamber volumes and recharge rates, the presence of an exsolved magmatic volatile phase hinders chamber growth because eruptive volumes are typically larger than recharges feeding the system during periods of dormancy. At pressures > *rsim*2.5 kbar, the viscosity of the crust in long-lived magmatic provinces is sufficiently low to inhibit most eruptions. Sustainable eruptible magma reservoirs are able to develop only within a relatively narrow range of pressures around 2 ± 0.5 kbar, where the amount of exsolved volatiles fosters growth while the high viscosity of the crust promotes the necessary overpressurization for eruption.

Over the last decades, a polybaric view of magmatic differentiation has emerged (see early ideas in refs. [1,2]), referred to as 'crustal distillation columns' with multiple levels of storage and differentiation[3]. However, the depth/pressure at which magmas stall and the processes that control those storage depths remain controversial[4]. Magmas are typically thought to accumulate first at the crust–mantle boundary, forming deep crustal mush zones (MASH[5] or hot zones[6]) and then again at shallow depths, potentially leading to two main storage levels[3]. However, other conceptual models have suggested several additional storage levels in the lower to middle crust[4,7].

Magma storage pressure is a fundamental variable that controls volatile exsolution and mineral phase assemblages, impacting chemical differentiation and eruptive styles of magmas as they ascend to the surface. Pressure is unfortunately one of the most difficult thermodynamic variables to constrain; its estimate by any method (for example, mineral barometry, volatile saturation pressures in melts or geophysical imaging of active systems) is subject to assumptions that can be challenging to validate. Here we present a complementary approach, focusing on mechanical processes thought to influence magma accumulation within the crust.

Crustal magma chambers—here defined as the eruptible portion of the magma reservoir—are thought to form by the amalgamation of sill- and dyke-like intrusions that transport magma vertically from deeper sources[8–10]. Therefore, understanding the depth at which these reservoirs form requires knowledge about the processes that cause dykes and sills to stall in the subsurface, and the processes that allow subsequent growth of the incipient magma reservoirs[11]. Dyke arrest and deflection into sills are largely governed by fracture mechanics, and some commonly cited controls include neutral buoyancy[12,13], rheological and rigidity contrasts[14,15], and reorientation of stresses[9]. Although dyke propagation occurs over short timescales where the host crust behaves elastically, the growth of subvolcanic magma chambers occurs on longer timescales allowing for ductile deformation of the crust to play a role. The observation that magma transport in the upper crust occurs by brittle deformation, while storage requires some amount of crustal creep, is the reason that the 'brittle–ductile' transition is commonly invoked as the primary control on the depth of silicic magma reservoirs (for example, refs. [16–18]).

Brittle–ductile transition and the depth of magma chambers

Within the context of the brittle–ductile transition, a magma chamber can grow if the crust can deform in a ductile manner in response to recharges, limiting the pressure build-up within the magma chamber and inhibiting eruptions. Although the brittle–ductile transition may influence the depth of emplacement of magma reservoirs, it is an incomplete argument. The rheology of the crust—whether it is brittle or ductile—depends not only on the temperature[19] but also on the strain rate. In the context of magma chamber growth, the strain rate is a function of the rate of pressure build-up in the magma chamber, which depends on the reservoir volume, compressibility and magma recharge rate[11]. Therefore, even considering the same crustal composition and temperature, the 'brittle–ductile transition' may occur at different depths for different rates of pressure loading in the chamber[20]. Moreover, the conditions required for magma chamber growth in erupting systems (mass loss at the surface) remain puzzling. Hence, we focus here on conditions required for magma chambers to grow while the system remains volcanically active.

We posit here that exsolved magmatic volatiles play an important role in the growth of subvolcanic chambers by regulating the size of eruptions. Chamber growth occurs by recharge (mass addition), and is limited by eruption (mass loss). The role of exsolved volatiles is key for eruption volume[21]; the presence of an exsolved volatile phase in the reservoir can significantly enhance the mass of magma erupted during a single event. Furthermore, three-phase

[1]Department of Earth, Environmental and Planetary Sciences, Brown University, Providence, RI, USA. [2]Department of Earth Sciences, University of Oregon, Eugene, OR, USA. [3]School of Earth and Ocean Sciences, Cardiff University, Cardiff, UK. [4]Department of Earth Sciences, ETH Zurich, Zurich, Switzerland. *e-mail: christian_huber@brown.edu

thermomechanical modelling of volcanic systems demonstrated that exsolved volatiles damp the build-up of pressure in shallow magma chambers caused by recharges during periods between eruptions[22,23]. The presence and exsolution of volatiles therefore exerts a fundamental control on the proportion of the magma emplaced in the chamber that is later erupted, and hence the propensity of magma chambers to grow, stall or shrink over time[21,24].

A multiphase framework for magma reservoir evolution is required to identify the conditions that are most favourable to the growth of large eruptible chambers of silicic magmas in the crust. The physical model used here includes visco-elastic rheology for the host response to pressure changes in the chamber and the evolution of an open multiphase magma chamber (crystal–melt–exsolved volatiles) in response to magma recharges, eruptions and cooling[25]. The model, based on mass and enthalpy conservation equations (see Supplementary Information), was run for more than 500 simulations initiated at a temperature of 930 °C, just below the magma liquidus (950 °C), and stopped when the magma reached a critical crystallinity of 50 vol%, where it is assumed no longer eruptible. These simulations cover a parameter space of initial magma water content that ranges from 4 to 7 wt% (increments of 1 wt%), lithostatic pressure from 1 to 3 kbar (increments of 0.25 kbar), initial chamber volumes ranging from 0.1 to 10 km^3 and long-term averaged magma recharge rates of 10^{-5} to 10^{-3} km^3 yr^{-1}. We consider a continuous and fixed set of recharge rates because our objective is to understand the growth and eruption behaviour of chambers over their lifespan rather than over a single recharge event and eruption cycle. The effect of short-term transient variations in recharge rate on magma chamber dynamics was studied in ref. [22].

The background geotherm (in the far-field) is set to 30 °C km^{-1}, such that the far-field temperature varies with the storage depth (a range of far-field geotherms is considered in the Supplementary Information). The temperature-dependent flow law used here for the rheology of the crust[26] is the same as the one previously used in thermomechanical models[27,28]. The goal of the simulations is to determine the subdomain in parameter space (initial chamber volume, recharge rate, depth and magma water content) where the following two conditions are satisfied: the magma chamber grows (by mass) over the course of the simulation and the magma chamber is capable of eruptions (mass withdrawal from the chamber). As such, we are not considering internal processes such as mixing or chemical zonation or stratification, but focus on the balance between pressure evolution, crustal response and crystallization–exsolution that is essential to characterize the long-term evolution (growth and eruption) of these magma bodies.

Grow versus blow

The processes that govern repose and eruption cycles at volcanoes are complex and tightly coupled. It is possible, however, to characterize the dynamics of a chamber subjected to magma injection and eruptions using a simplified framework that consists of three competing timescales[25]. The cooling timescale of a magma body is defined by $\tau_{cool} = R^2/\kappa$, with R being a characteristic length scale of the chamber (or effective radius) and κ being the thermal diffusivity of host rocks. This timescale controls the internal evolution of the magma chamber in terms of the volume fraction of melt, crystals and exsolved volatiles. By extension, it affects the thermal and mechanical response of the magma body to recharges and eruptions. The relaxation timescale $\tau_{relax} = \eta_{eff}/\Delta p_c$, where η_{eff} is the effective flow law of the crustal material evaluated at initial conditions (here taken from ref. [26]) and Δp_c is the critical overpressure that leads to eruptions. The relaxation timescale characterizes the ability of the crust to relax changes in pressure in the chamber by creep. The injection timescale $\tau_{inj} = M/\dot{M}_{inj}$, with $\dot{M}_{inj}$ being the mass influx rate of magma into the chamber and M being the mass of magma already present in the chamber. By convention, we report the injection rate in units of cubic kilometres per year for $\dot{M}_{inj}/\rho$, where ρ is the density of the magma injected.

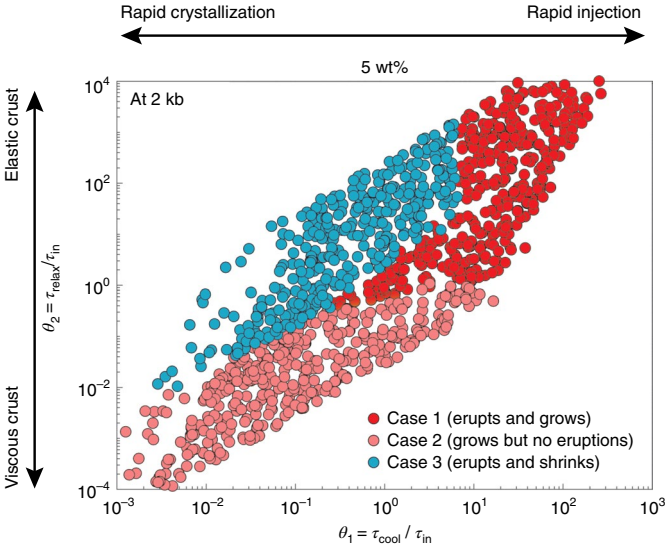

Fig. 1 | A regime diagram showing the evolution of magma chambers at a pressure of 2 kbar. The magma initially contains 5 wt% water. The *x* axis refers to the ratio of the cooling and injection timescales (more rapid injection rates to the right) and the *y* axis describes the ability of the crust to accommodate the mass change in the chamber (high = elastic behaviour of the crust, low ductile deformation). Additional simulations tested with a different critical overpressure (40 MPa) show a qualitatively similar behaviour with a slightly larger domain for simulations that undergo eruptions (case 1).

From these three timescales, we define two dimensionless ratios $\theta_1 = \tau_{cool}/\tau_{inj}$ (akin to a Peclet number) and $\theta_2 = \tau_{relax}/\tau_{inj}$ (akin to a Deborah number).

On the basis of several hundred simulations run at a fixed pressure of 2 kbar and considering a magma containing initially 5 wt% water (Fig. 1), three different regimes can be identified. In case 1, the chamber grows and erupts over the course of the simulation; this occurs when the injection timescale is smaller than both the relaxation and cooling timescales ($\theta_1 > 1$ and $\theta_2 > 1$). In case 2, the chamber grows but does not erupt, leading to the growth of plutonic roots. This regime occurs when the relaxation timescale is short compared to the injection timescale (crust is compliant and efficient at dissipating overpressure), and $\theta_2/\theta_1 < 1$. In case 3, the chamber erupts but is not long-lived (as much mass is erupted as added by recharges over time; $\theta_2 > 1$ and $\theta_1 < 1$).

The boundaries between these domains illustrate that both internal (heat loss causing crystallization and exsolution, and pressure increase by recharges) and external factors (rheology of the crust) control magma chamber growth and stability.

A sweet spot around 2 kbar

Running additional simulations over a range of depth (that is, lithostatic pressure and temperature) and magma water content values leads to three major observations (Fig. 2). First, some conditions of magma recharge and initial magma chamber size do not yield any parameter space for chambers simultaneously growing and erupting. This is true for large chambers and small recharge fluxes and it is consistent with recharges being too weak to trigger eruptions[25]. Second, the pressure range where magma chambers are found to grow while being tapped by eruptions (in red) is restricted to around 2 ± 0.5 kbar. Third, the boundary between eruptible and non-eruptible growing magma chambers (cases 1 and 2) is dominantly vertical to subvertical (that is, independent of the water content in the

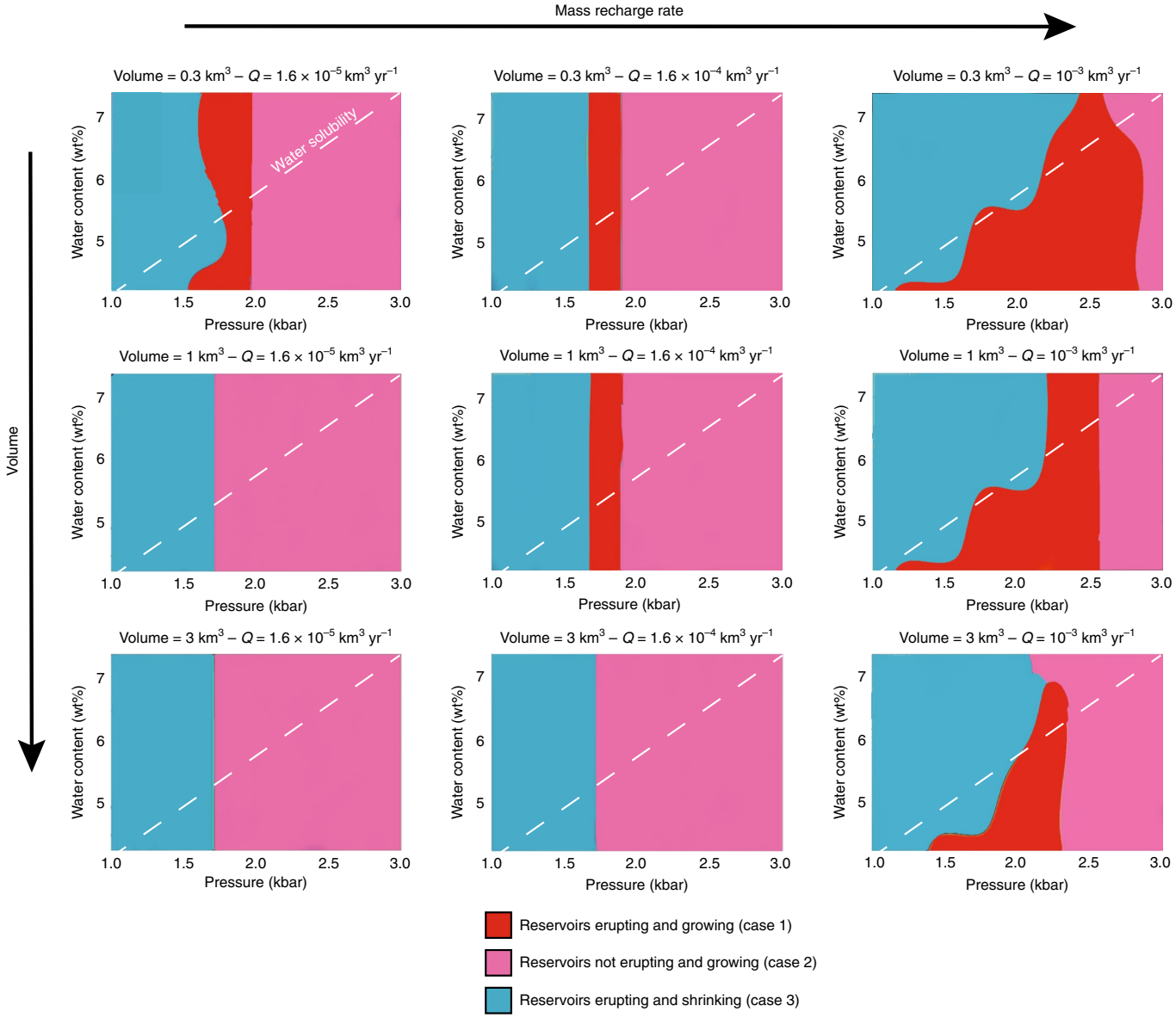

Fig. 2 | Regime diagrams of eruptible and growing chambers as a function of magma water content, depth, magma recharge rate and initial volume. Each plot shows three regions. The blue region represents conditions that are favourable for volcanic eruptions, but where the mass of magma stored shrinks with time (short-lived systems that cannot build up to large volumes). The red region highlights the regime where magma chambers are eruptible and grow. The pink region shows the regime where magma chambers grow, but do not erupt (they will ultimately form plutonic material). The white dashed line shows the water solubility curve (based on ref. [60]).

chamber), implying that the transition is largely independent of the internal state of the chamber; it is mostly controlled by the depth of the chamber, the size of the chamber and the magma recharge rate. As the recharge rate increases, the boundary shifts to greater depth because pressure build-up is more rapid and can compete with the timescale for the host rock to relax stress by creep. In contrast, at a given recharge rate and increasing chamber volume, the pressure build-up is slower and therefore more prone to be accommodated by creep in the host rocks (shallowing of the boundary between regimes).

The boundary that separates the two regimes of eruptible chambers (cases 1 and 3) at low pressure is also dominantly subvertical. At high water content (>5 wt% H_2O), saturation in a magmatic volatile phase is reached at or near the liquidus, while at slightly lower water content (~4 wt%), magmatic volatile phase saturation is reached after only a few tens of percent crystallization. This behaviour is consistent with the shallowing of the transition between growing and shrinking chambers to follow a trend subparallel to the slope of the solubility curve (white dashed line in Fig. 2) for chambers subjected to fast recharge rates and magmas with low water content.

The cause for overall mass loss in shallow chambers (<~1.5 kbar) is cooling and crystallization-driven exsolution during the interval between eruptions (dormancy periods). If a chamber can significantly exsolve volatiles during its repose phase, the eruption volume and mass can exceed the mass supplied by recharges (this is true for all recharge rates tested here). This also explains the shallowing of the transition at low water content, because the behaviour is mostly absent in chambers that do not undergo significant second boiling. In addition, the cooling caused by an eruption is more significant for chambers containing a significant mass of exsolved volatiles. The smaller erupting chambers will therefore also cool faster, creating a positive feedback that leads to rapid solidification.

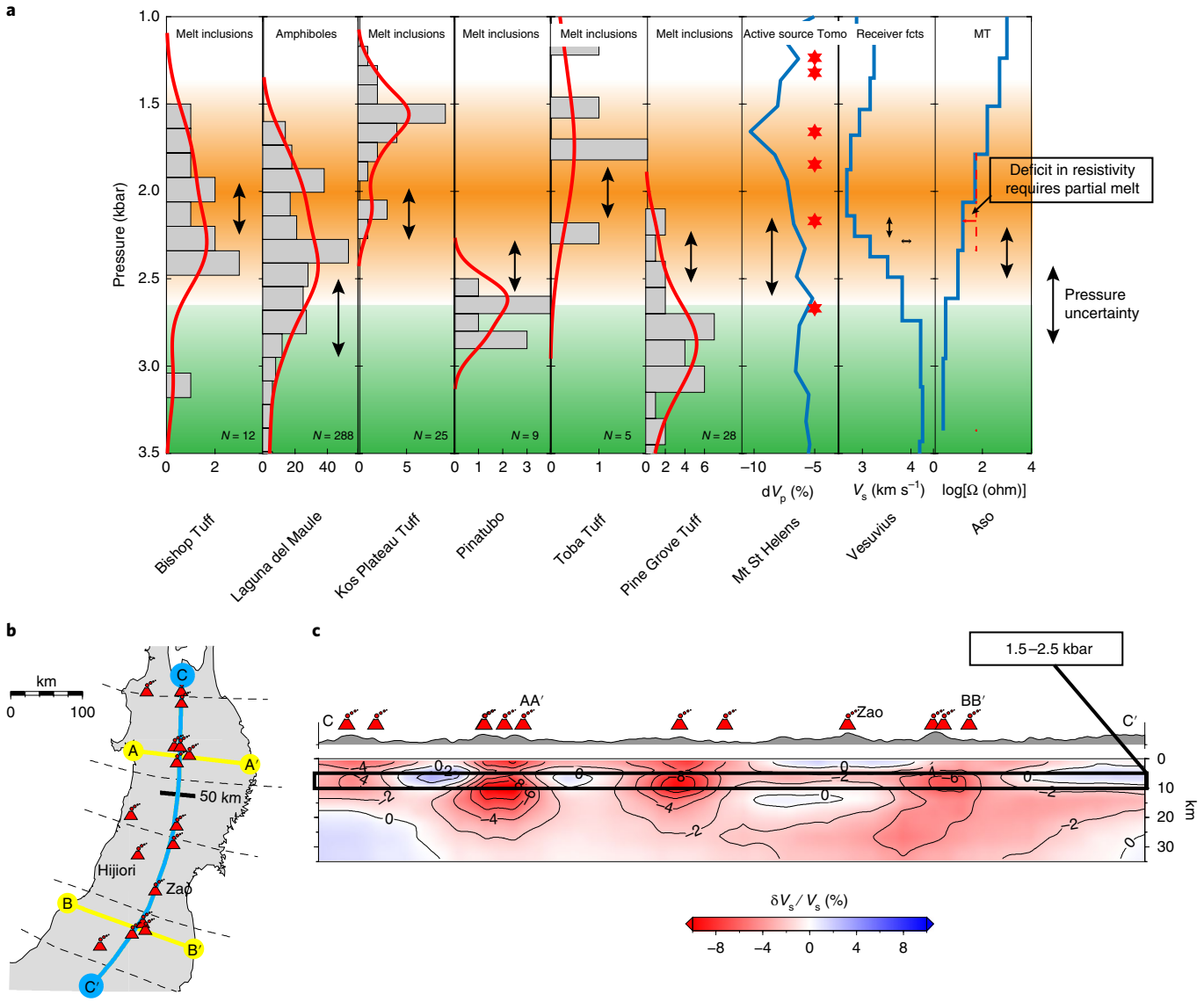

Fig. 3 | Pressure distribution where melt/active magma reservoir is inferred from petrology or geophysical methods. a, A comparison of petrological and geophysical datasets. The double-headed arrows represent pressure uncertainty as provided by the referenced studies: Bishop Tuff[39], Kos Plateau Tuff[37], Pinatubo[61], Toba Tuff[62] and Pine Grove[63] are estimates from melt inclusions (in quartz), and Laguna del Maule[58] from amphibole geobarometry. St Helens, Vesuvius and Aso pressure distributions are retrieved from geophysical inversion on V_p[53], V_s[64] and magnetotellurics[65]. The stars for St Helens refer to pressure estimates from experimental petrology[49,66]. Here, depth to pressure conversion assumes a crust with an average density of 2,750 kg m^{-3}. **b**,**c**, A map and V_s profile in northern Japan; adapted from ref. [67], Wiley.

Pressure at storage conditions

A large proportion of petrological studies rely on melt inclusion data or mineral barometry (see compilation by refs. [4,29–32]). However, trapping of melt inclusions typically occurs during rapid mineral growth, potentially leading to boundary layer effects[33] and behaviour as imperfect pressure vessels, especially in mineral phases that cleave or crack easily (such as plagioclases or pyroxenes). During decompression associated with eruptions, melt inclusions can leak and record low pressures that may not relate to the reservoir conditions (for example, recording depths of <2–3 km; refs. [34–36]). For silicic magmas, studies that report compositions of pristine quartz-hosted melt inclusions probably provide the most reliable pressure estimates (for example, refs. [37–39]). Similarly, mineral barometry suffers from inaccuracies related to the fact that compositional parameters in minerals are not only pressure sensitive, but also strongly depend on temperature and melt composition. For example, when amphibole phenocrysts grow from a melt that is saturated with multiple other phases (such as quartz, biotite, 2 feldspars), then the degrees of freedom in the melt composition are limited (the system is compositionally buffered), and pressure values tend to be more reliable using the latest barometric calculations (see, for example, refs. [40,41]). However, when magmas have less mineral diversity, amphibole compositions can strongly vary as a function of melt composition, and barometric calculations can be unreliable[30,42].

Constraining the volume and depth of shallow magma chambers from geophysical images is also challenging because resolution is typically low, and active volcanoes often host a hydrothermal system above the reservoir, where hot fluids circulate in the permeable crust[18]. From geophysical inversions, hydrothermal systems are not easy to distinguish from regions where silicate melt accumulates, because both share similar signatures (density significantly lower than that of the surrounding crust, high electric conductivity,

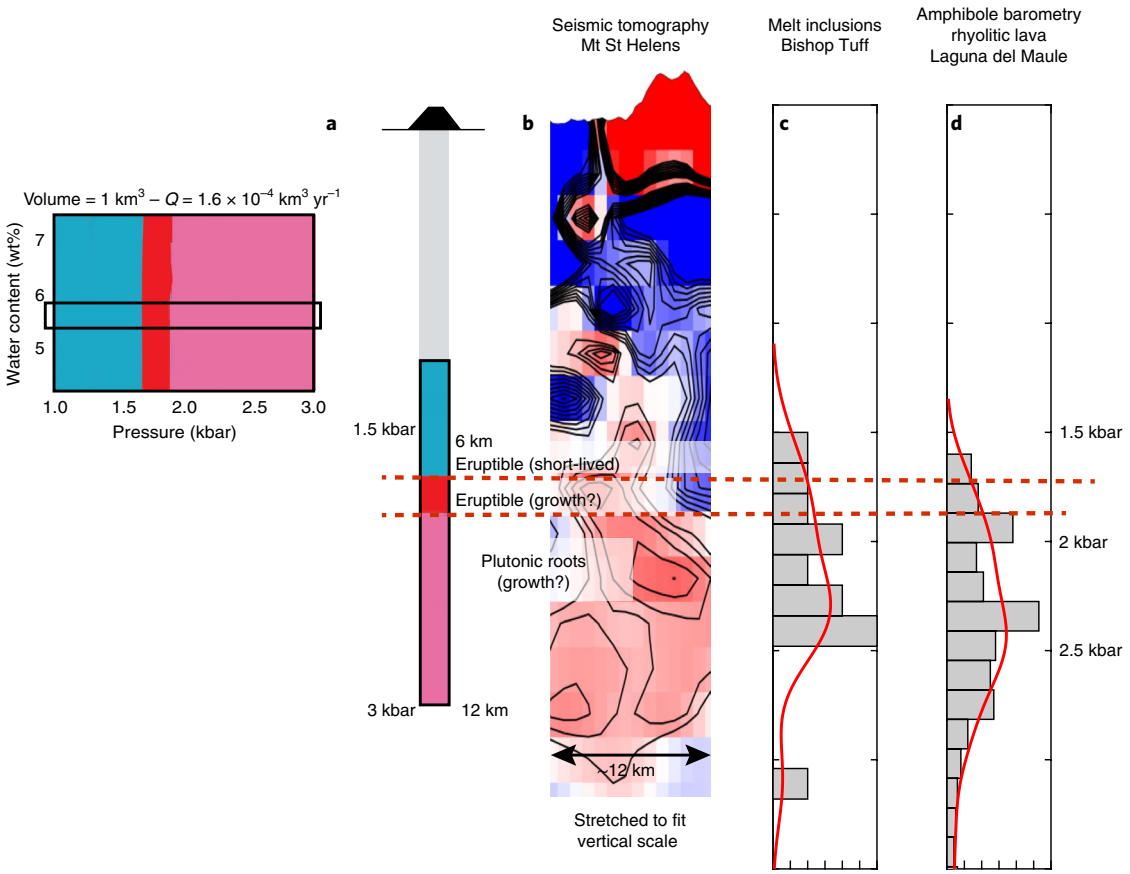

Fig. 4 | A summary diagram comparing numerical simulations with geophysical and petrological data. a–d, An example from a numerical simulation of Fig. 2 (**a**) compared with seismic tomography (active) at Mt St Helens[53] (**b**), melt inclusion data from the Bishop Tuff, Long Valley Caldera[39] (**c**) and amphibole geobarometry at Laguna del Maule, Chile[58] (**d**).

low shear velocity (V_s) and high ratio of primary to shear wave velocity (V_p/V_s); for example, refs. [43–45]). Similarly, during unrest periods at a volcanic edifice, it is expected that the hydrothermal circulation and possibly boiling of water can lead to pressure changes that are detected by geodetic surveys[46,47], leading again to a bias for shallow structures.

With these caveats in mind, we summarize published petrologic and geophysical data on storage depths for various volcanic centres (Fig. 3). While this is not an exhaustive list, the data presented follow the selection criteria discussed above (for example, quartz-hosted melt inclusions, pristine amphibole composition with buffering mineral assemblage and well-characterized experimental constraints). All three independent techniques (mineral and melt inclusion barometry and geophysical imaging) converge towards an average pressure of 2 ± 0.5 kbar for the emplacement of the subvolcanic reservoirs that feed most intermediate to silicic eruptions. This optimal pressure range is well known to experimental petrologists, who commonly use 2 kbar as the default pressure for many of their runs[48–50]. This observation holds true across tectonic settings, and all differentiation trends.

Evolution and imaging of magmatic columns

Our model results provide a process-based understanding of several important aspects of polybaric evolution in water-rich silicic magma chambers in the middle to upper crust. These chambers are able to form around pressures of about 1.5–2.5 kbar because the crust is compliant enough to host growing magma bodies and the abundance of exsolved volatiles and efficiency of exsolution is limited enough for eruptions not to mobilize more magma than what is supplied. Interestingly, although magma chambers are able to grow more efficiently at pressures above 2.5 kbar in our model, the magma emplaced at these depths or deeper generally does not contribute directly to the volcanic record unless exceptionally large recharge rates are considered (long-term averaged fluxes $>>10^{-3}$ km^3 yr^{-1}).

Our simulations suggest that only transient magma bodies (unable to grow to any significant size) form at pressures below 1.5 kbar; eruptible and long-lived (potentially large) bodies form between 1.5 and 2.5 kbar; and large non-eruptible roots (that may supply shallower systems) emplace beyond 2.5 kbar, in excellent agreement with experimental petrology[51,52], observations from geophysical imaging[53–57], melt inclusion data[37,39] and mineral and melt barometry[58,59] for different silicic volcanic centres that are capable of eruption volumes spanning 3 orders of magnitude (Fig. 4). With variable tectonic stresses, as well as magma and volatile compositions, the pressure bounds (here suggested to be ~1.5 to 2.5 kbar) will change slightly, but the existence of an optimal entrapment depth in the upper crust for erupting reservoirs will abide.

Online content

Any methods, additional references, Nature Research reporting summaries, source data, statements of code and data availability and associated accession codes are available at https://doi.org/10.1038/s41561-019-0415-6.

Received: 30 December 2018; Accepted: 25 June 2019;
Published online: 19 August 2019

References

1. Hildreth, W. Gradients in silicic magma chambers: implications for lithospheric magmatism. *J. Geophys. Res.* **86**, 10153–10192 (1981).
2. Lipman, P. W., Doe, B. & Hedge, C. Petrologic evolution of the San Juan volcanic field, southwestern Colorado: Pb and Sr isotope evidence. *Geol. Soc. Am. Bull.* **89**, 59–82 (1978).
3. Bachmann, O. & Huber, C. Silicic magma reservoirs in the Earth's crust. *Am. Mineral.* **101**, 2377–2404 (2016).
4. Cashman, K. V., Sparks, R. S. J. & Blundy, J. D. Vertically extensive and unstable magmatic systems: a unified view of igneous processes. *Science* **355**, eaag3055 (2017).
5. Hildreth, W. S. & Moorbath, S. Crustal contributions to arc magmatism in the Andes of central Chile. *Contrib. Mineral. Petrol.* **98**, 455–499 (1988).
6. Annen, C., Blundy, J. D. & Sparks, R. S. J. The genesis of intermediate and silicic magmas in deep crustal hot zones. *J. Petrol.* **47**, 505–539 (2006).
7. Marsh, B. D. A magmatic mush column Rosetta Stone: the McMurdo Dry Valleys of Antarctica. *EOS Trans. Am. Geophys. Union* **85**, 497–502 (2004).
8. Burchardt, S. New insights into the mechanics of sill emplacement provided by field observations of the Njardvik Sill, Northeast Iceland. *J. Volcanol. Geotherm. Res.* **173**, 280–288 (2008).
9. Menand, T. Physical controls and depth of emplacement of igneous bodies: a review. *Tectonophysics* **500**, 11–19 (2011).
10. Miller, C. F. et al. Growth of plutons by incremental emplacement of sheets in crystal-rich host: evidence from Miocene intrusions of the Colorado River region, Nevada, USA. *Tectonophysics* **500**, 65–77 (2011).
11. Karlstrom, L., Paterson, S. R. & Jellinek, A. M. A reverse energy cascade for crustal magma transport. *Nat. Geosci.* **10**, 604–608 (2017).
12. Lister, J. R. & Kerr, R. C. Fluid-mechanical models of crack propagation and their application to magma transport in dykes. *J. Geophys. Res. Solid Earth* **96**, 10049–10077 (1991).
13. Walker, G. P. L. Gravitational (density) controls on volcanism, magma chambers and intrusions. *Aust. J. Earth Sci.* **36**, 149–165 (1989).
14. Gudmundsson, A. Magma chambers: formation, local stresses, excess pressures, and compartments. *J. Volcanol. Geotherm. Res.* **237–238**, 19–41 (2012).
15. Rivalta, E., Taisne, B., Bunger, A. P. & Katz, R. F. A review of mechanical models of dike propagation: schools of thought, results and future directions. *Tectonophysics* **638**, 1–42 (2015).
16. Burov, E., Jaupart, C. & Guillou-Frottier, L. Ascent and emplacement of buoyant magma bodies in brittle–ductile upper crust. *J. Geophys. Res.* **108**, 2177 (2003).
17. Gregg, P. M., de Silva, S. L., Grosfils, E. B. & Parmigiani, J. P. Catastrophic caldera-forming eruptions: thermomechanics and implications for eruption triggering and maximum caldera dimensions on Earth. *J. Volcanol. Geotherm. Res.* **241–242**, 1–12 (2012).
18. Lowenstern, J. B., Smith, R. B. & Hill, D. P. Monitoring super-volcanoes: geophysical and geochemical signals at Yellowstone and other large caldera systems. *Phil. Trans. R. Soc. A* **364**, 2055–2072 (2006).
19. Gettings, M. E. Variation of depth to the brittle–ductile transition due to cooling of a midcrustal intrusion. *Geophys. Res. Lett.* **15**, 213–216 (1988).
20. Rubin, A. M. Dike ascent in partially molten rock. *J. Geophys. Res. Solid Earth* **103**, 20901–20919 (1998).
21. Huppert, H. E. & Woods, A. W. The role of volatiles in magma chamber dynamics. *Nature* **420**, 493–495 (2002).
22. Degruyter, W., Huber, C., Bachmann, O., Cooper, K. M. & Kent, A. J. R. Magma reservoir response to transient recharge events: the case of Santorini volcano (Greece). *Geology* **44**, 23–26 (2016).
23. Degruyter, W., Huber, C., Bachmann, O., Cooper, K. M. & Kent, A. J. R. Influence of exsolved volatiles on reheating silicic magmas by recharge and consequences for eruptive style at Volcán Quizapu (Chile). *Geochem. Geophys. Geosyst.* **18**, 4123–4135 (2017).
24. Forni, F., Degruyter, W., Bachmann, O., De Astis, G. & Mollo, S. Long-term magmatic evolution reveals the beginning of a new caldera cycle at Campi Flegrei. *Sci. Adv.* **4**, eaat940 (2018).
25. Degruyter, W. & Huber, C. A model for eruption frequency of upper crustal silicic magma chambers. *Earth Planet. Sci. Lett.* **403**, 117–130 (2014).
26. Hansen, F. D. & Carter, N. L. Semibrittle creep of dry and wet westerly granite at 1,000 MPa. In *The 24th US Symposium on Rock Mechanics* 20 (American Rock Mechanics Association, 1983).
27. Jellinek, A. M. & DePaolo, D. J. A model for the origin of large silicic magma chambers: precursors of caldera-forming eruptions. *Bull. Volcanol.* **65**, 363–381 (2003).
28. Karlstrom, L., Dufek, J. & Manga, M. Magma chamber stability in arc and continental crust. *J. Volcanol. Geotherm. Res.* **190**, 249–270 (2010).
29. Johnson, M. C. & Rutherford, M. J. Experimental calibration of the aluminum-in-hornblende geobarometer with application to Long Valley Caldera (California) volcanic rocks. *Geology* **17**, 837–841 (1989).
30. Putirka, K. Amphibole thermometers and barometers for igneous systems and some implications for eruption mechanisms of felsic magmas at arc volcanoes. *Am. Mineral.* **101**, 841–858 (2016).
31. Schmidt, M. W. Amphibole composition in tonalite as a function of pressure; an experimental calibration of the Al-in-hornblende barometer. *Contrib. Mineral. Petrol.* **110**, 304–310 (1992).
32. Wallace, P. J., Anderson, A. T. & Davis, A. M. Quantification of pre-eruptive exsolved gas contents in silicic magmas. *Nature* **377**, 612–615 (1995).
33. Baker, D. R. The fidelity of melt inclusions as records of melt composition. *Contrib. Mineral. Petrol.* **156**, 377–395 (2008).
34. Blundy, J. D. & Cashman, K. V. Rapid decompression-driven crystallization recorded by melt inclusions from Mount St. Helens volcano. *Geology* **33**, 793–796 (2005).
35. Lloyd, A. S., Plank, T., Ruprecht, P., Hauri, E. H. & Rose, W. Volatile loss from melt inclusions in pyroclasts of differing sizes. *Contrib. Mineral. Petrol.* **165**, 129–153 (2013).
36. Wallace, P. in *Melt Inclusions in Volcanic Systems: Methods, Applications and Problems* Vol. 5 (eds De Vivo, B. & Bodnar, R. J.) 105–127 (Elsevier, 2003).
37. Bachmann, O., Wallace, P. J. & Bourquin, J. The melt inclusion record from the rhyolitic Kos Plateau Tuff (Aegean Arc). *Contrib. Mineral. Petrol.* **159**, 187–202 (2010).
38. Lowenstern, J. B. in *Melt Inclusions in Volcanic Systems: Methods, Applications and Problems* Vol. 5 (eds De Vivo, B. & Bodnar, R. J.) 1–22 (Elsevier, 2003).
39. Wallace, P. J., Anderson, A. T. & Davis, A. M. Gradients in H_2O, CO_2, and exsolved gas in a large-volume silicic magma chamber: interpreting the record preserved in the melt inclusions from the Bishop Tuff. *J. Geophys. Res.* **104**, 20097–20122 (1999).
40. Ague, J. J. Thermodynamic calculation of emplacement pressures for batholithic rocks, California; implications for the aluminum-in-hornblende barometer. *Geology* **25**, 563–566 (1997).
41. Bachmann, O. & Dungan, M. A. Temperature-induced Al-zoning in hornblendes of the Fish Canyon magma, Colorado. *Am. Mineral.* **87**, 1062–1076 (2002).
42. Erdmann, S., Martel, C., Pichavant, M. & Kushnir, A. Amphibole as an archivist of magmatic crystallization conditions: problems, potential, and implications for inferring magma storage prior to the paroxysmal 2010 eruption of Mount Merapi, Indonesia. *Contrib. Mineral. Petrol.* **167**, 1–23 (2014).
43. Bedrosian, P. A., Peacock, J. R., Bowles-Martinez, E., Schultz, A. & Hill, G. J. Crustal inheritance and a top-down control on arc magmatism at Mount St Helens. *Nat. Geosci.* **11**, 865–870 (2018).
44. Hata, M., Takakura, S., Matsushima, N., Hashimoto, T. & Utsugi, M. Crustal magma pathway beneath Aso caldera inferred from three-dimensional electrical resistivity structure. *Geophys. Res. Lett.* **43**, 10,720–10,727 (2016).
45. Miller, C. A., Le Mével, H., Currenti, G., Williams-Jones, G. & Tikoff, B. Microgravity changes at the Laguna del Maule volcanic field: magma-induced stress changes facilitate mass addition. *J. Geophys. Res. Solid Earth* **122**, 3179–3196 (2017).
46. Chaussard, E. & Amelung, F. Regional controls on magma ascent and storage in volcanic arcs. *Geochem. Geophys. Geosyst.* **15**, 1407–1418 (2014).
47. Hurwitz, S., Kipp, K. L., Ingebritsen, S. E. & Reid, M. E. Groundwater flow, heat transport, and water table position within volcanic edifices: implications for volcanic processes in the Cascade Range. *J. Geophys. Res. Solid Earth* **108**, 2557 (2003).
48. Holtz, F., Sato, H., Lewis, J. F., Behrens, H. & Nakada, S. Experimental petrology of the 1991–1995 Unzen Dacite, Japan. Part I: phase relations, phase composition and pre-eruptive conditions. *J. Petrol.* **46**, 319–337 (2005).
49. Rutherford, M. J., Sigurdsson, H., Carey, S. & Davis, A. M. The May 18, 1980, eruption of Mount St. Helens, 1. Melt composition and experimental phase equilibria. *J. Geophys. Res.* **90**, 2929–2947 (1985).
50. Scaillet, B., Holtz, F. & Pichavant, M. Experimental constraints on the formation of silicic magmas. *Elements* **12**, 109–114 (2016).
51. Johnson, M. & Rutherford, M. Experimentally determined conditions in the Fish Canyon Tuff, Colorado, magma chamber. *J. Petrol.* **30**, 711–737 (1989).
52. Scaillet, B. & Evans, B. W. The 15 June 1991 eruption of Mount Pinatubo. I. Phase equilibria and pre-eruption P–*T*–fO_2–fH_2O conditions of the dacite magma. *J. Petrol.* **40**, 381–411 (1999).
53. Kiser, E., Levander, A., Zelt, C., Schmandt, B. & Hansen, S. M. Focusing of melt near the top of the Mount St. Helens (USA) magma reservoir and its relationship to major volcanic eruptions. *Geology* **46**, 775–778 (2018).
54. Huang, H.-H. et al. The Yellowstone magmatic system from the mantle plume to the upper crust. *Science* **348**, 773–776 (2015).
55. Huang, Y.-C., Ohkura, T., Kagiyama, T., Yoshikawa, S. & Inoue, H. Shallow volcanic reservoirs and pathways beneath Aso caldera revealed using ambient seismic noise tomography. *Earth Planets Space* **70**, 169 (2018).
56. Masturyono, McCaffrey, R., Wark, D. A. & Roecker, S. W. Distribution of magma beneath the Toba caldera complex, north Sumatra, Indonesia, constrained by three-dimensional P wave velocities, seismicity, and gravity data. *Geochem. Geophys. Geosyst.* **2**, 2000GC000096 (2001).
57. Fedi, M. et al. Gravity modeling finds a large magma body in the deep crust below the Gulf of Naples, Italy. *Sci. Rep.* **8**, 8229 (2018).

58. Andersen, N. L. et al. Pleistocene to Holocene growth of a large upper crustal rhyolitic magma reservoir beneath the active Laguna del Maule volcanic field, central Chile. *J. Petrol.* **58**, 85–114 (2017).
59. Gualda, G. A. R. & Ghiorso, M. S. Low-pressure origin of high-silica rhyolites and granites. *J. Geol.* **121**, 537–545 (2013).
60. Liu, Y., Zhang, Y. & Behrens, H. Solubility of H_2O in rhyolitic melts at low pressures and a new empirical model for mixed H_2O–CO_2 solubility in rhyolitic melts. *J. Volcanol. Geotherm. Res.* **143**, 219–235 (2005).
61. Wallace, P. J. & Gerlach, T. M. Magmatic vapor source for sulfur dioxide released during volcanic eruptions: evidence from Mount Pinatubo. *Science* **265**, 497–499 (1994).
62. Chesner, C. A. & Luhr, J. F. A melt inclusion study of the Toba Tuffs, Sumatra, Indonesia. *J. Volcanol. Geotherm. Res.* **197**, 259–278 (2010).
63. Lowenstern, J. B., Bacon, C. R., Calk, L. C., Hervig, R. L. & Aines, R. D. *Major-Element, Trace-Element, and Volatile Concentrations in Silicate Melt Inclusions from the Tuff of Pine Grove, Wah Wah Mountains, Utah* Open-File Report 94-242 (US Geological Survey, 1994).
64. Agostinetti, N. P. & Chiarabba, C. Seismic structure beneath Mt Vesuvius from receiver function analysis and local earthquakes tomography: evidences for location and geometry of the magma chamber. *Geophys. J. Int.* **175**, 1298–1308 (2008).
65. Hata, M. et al. Three-dimensional electrical resistivity distribution beneath the Beppu–Shimabara graben with a focus on Aso caldera, Southwest Japan subduction zone. *J. Geophys. Res. Solid Earth* **123**, 6397–6410 (2018).
66. Gardner, J. E., Carey, S., Rutherford, M. J. & Sigurdsson, H. Petrologic diversity in Mount St-Helens dacites during the last 4,000 years - implications for magma mixing. *Contrib. Mineral. Petrol.* **119**, 224–238 (1995).
67. Chen, K.-X., Gung, Y., Kuo, B.-Y. & Huang, T.-Y. Crustal magmatism and deformation fabrics in northeast Japan revealed by ambient noise tomography. *J. Geophys. Res. Solid Earth* **123**, 8891–8906 (2018).

Acknowledgements

The authors would like to thank K.-X. Chen for providing Fig. 3b,c in a format that allowed us to modify the figure. C.H. is funded through an NSF CAREER grant, M.T. is funded through NSF-EAR 1760004 awarded to C.H., and O.B. is funded by the Swiss National Fund 200021_178928. The authors dedicate this paper to the memory of our colleague and friend James Dale Webster.

Author contributions

C.H. and O.B. conceived the study with valuable inputs from M.T. and W.D. The numerical model was developed by C.H., W.D. and M.T. The analysis of the results was conducted by C.H. and M.T. and the initial draft of the manuscript was written by C.H. with improvements and substantial edits from M.T., W.D. and O.B.

Competing interests

The authors declare no competing interests.

Additional information

Supplementary information is available for this paper at https://doi.org/10.1038/s41561-019-0415-6.

Reprints and permissions information is available at www.nature.com/reprints.

Correspondence and requests for materials should be addressed to C.H.

Publisher's note: Springer Nature remains neutral with regard to jurisdictional claims in published maps and institutional affiliations.

Methods

The physical model is based on the conservation of total mass, water and enthalpy in a homogeneous magma chamber (see ref. [25]). The overpressure threshold set for the initiation of dykes was 20 MPa, but similar results were obtained with 40 MPa. The datasets generated during this study (outputs from numerical simulations) and the codes used to generate the results are available from the corresponding author.

Model description. We use the physical model developed by Degruyter and Huber[25] and extended by Townsend et al.[68] to describe the evolution of a magma reservoir. The model is designed to study the interaction of first-order processes that govern the capability for a magma reservoir to grow and erupt during its lifetime. The model considers an eruptible portion of magma referred to as the magma chamber sitting in a colder, viscoelastic region that represents the transition from a mush in the proximity of the chamber to the surrounding crust in the far field. We assume that the main processes involved are: magma recharge; crystallization; volatile exsolution; heat loss to the surroundings; viscoelastic response of the surroundings in response to volume changes in the chamber; and mass withdrawal due to eruptions (Supplementary Fig. 1).

Governing equations. The governing equations of the model are conservation of mass, water and energy applied to the magma chamber, which we can write concisely as:

$$\frac{\mathrm{d}M}{\mathrm{d}t} = \dot{M}_{\mathrm{in}} - \dot{M}_{\mathrm{out}} \tag{1}$$

$$\frac{\mathrm{d}M^{\mathrm{w}}}{\mathrm{d}t} = \dot{M}^{\mathrm{w}}_{\mathrm{in}} - \dot{M}^{\mathrm{w}}_{\mathrm{out}} \tag{2}$$

$$\frac{\mathrm{d}H}{\mathrm{d}t} = \dot{H}_{\mathrm{in}} - \dot{H}_{\mathrm{out}} \tag{3}$$

where M, M^{w} and H represent the (total) mass, the water mass and the enthalpy of the magma chamber, respectively. The subscripts 'in' and 'out' indicate source and sink terms, respectively.

Constitutive equations. The time evolution of the magma chamber volume (V), melt (ρ_{m}) and crystal density (ρ_{X}) are described by the following relationships:

$$\frac{\mathrm{d}V}{\mathrm{d}t} = \frac{1}{\beta_{\mathrm{r}}}\frac{\mathrm{d}P}{\mathrm{d}t} + \frac{\Delta P}{\eta_{\mathrm{r}}} - \alpha_{\mathrm{r}}\frac{\mathrm{d}T}{\mathrm{d}t} \tag{4}$$

$$\frac{\mathrm{d}\rho_{\mathrm{m}}}{\mathrm{d}t} = \frac{1}{\beta_{\mathrm{m}}}\frac{\mathrm{d}P}{\mathrm{d}t} - \alpha_{\mathrm{m}}\frac{\mathrm{d}T}{\mathrm{d}t} \tag{5}$$

$$\frac{\mathrm{d}\rho_{\mathrm{X}}}{\mathrm{d}t} = \frac{1}{\beta_{\mathrm{X}}}\frac{\mathrm{d}P}{\mathrm{d}t} - \alpha_{\mathrm{X}}\frac{\mathrm{d}T}{\mathrm{d}t} \tag{6}$$

where T is the temperature and P is the pressure in the chamber. α and β are the thermal expansion coefficient ($10^{-5}\,\mathrm{K}^{-1}$) and bulk modulus (10^{10} Pa), respectively. The subscripts m, X and r refer to the melt phase, crystal phase and mush/country rocks, respectively. ΔP indicates the overpressure (that is, the chamber pressure minus the lithostatic pressure). η_{r} is the effective viscosity of the surrounding shell.

The crystallization in the chamber is described by a parameterized relationship between the temperature and the crystal volume fraction defined by equation (13) in Huber et al.[69]. We use an exponent of $b = 0.5$, 700 °C for the solidus and 950 °C for the liquidus temperature, which are values representative for silicic magmas. We assume that water is the dominant volatile species. We use the solubility model of Zhang[70] as parameterized in equation (16) of Dufek and Bergantz[71], suitable for water in rhyolite. To determine the density of the exsolved volatile phase, we use the modified Redlich–Kwong relationship of Halbach and Chatterjee[72] as parameterized in equation (7) of Huber et al.[73].

Boundary conditions. We assume that magma is supplied continuously from deeper levels in the crust at a constant rate, which we vary between 10^{-5} and $10^{-3}\,\mathrm{km^3\,yr^{-1}}$ in agreement with long-term rates suggested for volcanic systems[74]. The temperature of the injected magma is assumed to be 927 °C (1,200 K) and its water content is equal to the initial water content of the chamber.

Mass withdrawal due to eruptions occurs when overpressure in the magma chamber reaches a critical overpressure of 20 MPa (40 MPa was also tested and led to similar results). The value of a critical overpressure is uncertain and has been suggested to fall anywhere between 1 and 100 MPa (ref. [14]). The values we use here are based on scaling arguments based on the cooling of a dyke[27,75]. We also require that the magma remains mobile for an eruption to occur. The physical properties of the magma removed from the chamber are set equal to those within the chamber. We simply set this criterion equivalent to having less than or equal to 0.5 crystal volume fraction, a value that is commonly used[76]. Once this crystal volume fraction is reached through sufficient cooling, the calculation is stopped.

The heat loss from the chamber to the surroundings is determined at each time step from an analytical solution whereby the chamber is considered to be a hot sphere sitting in a larger sphere with a radius ten times the radius of the initial chamber. The initial temperature profile between the inner and outer sphere is assumed to be at steady state and thus assumes a mature plumbing system. The temperature at the inner boundary is that of the magma chamber and that at the outer boundary is set at a constant value in accordance with the crustal temperature in the far field at the depth of the magma chamber. To obtain this temperature, we assume a geothermal gradient of $30\,^{\circ}\mathrm{C\,km^{-1}}$ for all of the calculations in the main paper. In the next section, we examine the influence of a hotter geotherm ($40\,^{\circ}\mathrm{C\,km^{-1}}$), as well as varying this temperature independently from the assumed depth of the chamber. The temperature profile evolves over time in response to changes in the temperature of the magma chamber taking into account the history of the temperature changes (see appendix A.4 in Degruyter and Huber[25]). From this profile, the heat flow rate emanating from the chamber is calculated.

The temperature profile of the shell is also used to determine η_{r}, the effective viscosity of the surrounding shell. At each position z in the shell, a viscosity $\eta(z)$ is determined using an Arrhenius law

$$\eta(z) = A\mathrm{e}^{\left(\frac{G}{BT(z)}\right)} \tag{7}$$

where $A = 4.27\times10^{7}$ Pa s is a material-dependent constant, $G = 141\times10^{3}\,\mathrm{J\,mol^{-1}}$ is the activation energy for creep flow, $B = 8.31\,\mathrm{J\,mol^{-1}\,K^{-1}}$ is the molar gas constant and $T(z)$ is the temperature at that position in the shell. We base equation (7) on the discussion of ref. [27] that uses values for Westerly granite with 0.1 wt% water based on experiments from Hansen and Carter[26]. The effective viscosity of the shell is calculated from averaging across the radially varying viscosity within the shell following the method of Lensky et al.[77]. See appendix A.5 in Degruyter and Huber[25] for further details.

Initial conditions. Together with the recharge rate, three initial conditions are varied to explore the parameter space. The initial pressure is set equal to the lithostatic pressure. Assuming a crustal density of $2{,}750\,\mathrm{kg\,m^{-3}}$ and a storage depth between 6 and 12 km, we evaluate storage pressure between 1 and 3 kbar. The choice of depth also determines the temperature of the outer shell of the surroundings, which is calculated using the geothermal gradient as discussed in the previous section. The initial volume of the chamber ranges between 0.1 and $10\,\mathrm{km^3}$ and the initial magma water content ranges from 4 to 7 wt%. The initial temperature and density of the melt and crystal phase are the same for all calculations and are 927 °C (1,200 K), $2{,}400\,\mathrm{kg\,m^{-3}}$ and $2{,}600\,\mathrm{kg\,m^{-3}}$, respectively.

The effect of different crustal geotherms. We ran additional simulations with a hotter far-field geotherm to test how it influences the most favourable depth of emplacement of a magma reservoir over various conditions (depth, water content in the magma, initial volume and recharge rate). It is important to note, however, that the near-field temperature field around the chamber (here, near field refers to a distance shorter than ten times the chamber radius) is initially set to be at steady-state with the hot magma reservoir (thermally mature crust) and is solved analytically accounting for the temperature variation in the chamber at any subsequent time. The far-field geotherm is therefore influencing the boundary condition in the far field alone. As expected, the results obtained with a hotter geotherm of $40\,^{\circ}\mathrm{C\,km^{-1}}$ are very similar to the results we obtained with $30\,^{\circ}\mathrm{C\,km^{-1}}$. The main difference is that the maximum depth for an eruptible magma reservoir is shallower (lower pressure) for the higher geotherm simulations, as expected.

We conducted a series of magma chamber simulations to establish whether the sweet spot observed in Fig. 2 and Supplementary Fig. 2 (in pressure or depth range, where magma chambers can both grow and erupt) is robust when considering a wide range of pressure–temperature (P–T) crustal conditions (Supplementary Figs. 3 and 4 show results for an initial magma water content of 4 and 6 wt%, respectively). The temperature on the x axis in these figures corresponds to the temperature assumed at the outer boundary of the surrounding shell as explained in the section above entitled Boundary conditions. This is equivalent to the 'unperturbed' crustal temperature at the same depth as the centroid of the magma chamber in the far field. Some of the most extreme P–T conditions explored are not realistic and we bracketed the most likely conditions between two endmember geotherms of 30 and $50\,^{\circ}\mathrm{C\,km^{-1}}$. In all cases, we observe that magma chambers shrink in mass at the lowest pressure (in general, a depth corresponding to pressures below 1.5 kbar) while growth (by mass) is promoted at higher pressure. We also find that eruptions are suppressed over the range of tested recharge rates when the far-field crustal temperature at an equivalent depth exceeds a critical temperature that ranges between 250 and 375 °C. The variation in critical temperature and pressure marking the transition from an eruptible to a non-eruptible chamber is mostly driven by the size and recharge rate of the chamber, which again supports the importance of conditions such as the volume of the chamber and the recharge rate of the magma on the brittle–ductile transition.

Data availability

The datasets generated during this study (outputs from numerical simulations) are available from the corresponding author on request.

Code availability

The code used to generate the magma chamber growth outputs can be accessed by contacting the corresponding author.

References

68. Townsend, M., Huber, C., Degruyter, W. & Bachmann, O. Magma chamber growth during intercaldera periods: insights from thermo-mechanical modeling with applications to Laguna del Maule, Campi Flegrei, Santorini, and Aso. *Geochem. Geophys. Geosyst.* **20**, 1574–1591 (2019).
69. Huber, C., Bachmann, O. & Manga, M. Homogenization processes in silicic magma chambers by stirring and mushification (latent heat buffering). *Earth Planet. Sci. Lett.* **283**, 38–47 (2009).
70. Zhang, Y. H_2O in rhyolitic glasses and melts: measurement, speciation, solubility, and diffusion. *Rev. Geophys.* **37**, 493–516 (1999).
71. Dufek, J. & Bergantz, G. W. Transient two-dimensional dynamics in the upper conduit of a rhyolitic eruption: a comparison of closure models for the granular stress. *J. Volcanol. Geotherm. Res.* **143**, 113–132 (2005).
72. Halbach, H. & Chatterjee, N. D. An empirical Redlich–Kwong equation of state for water to 1000 °C and 200 kbar. *Contrib. Mineral. Petrol.* **79**, 337–345 (1982).
73. Huber, C., Bachmann, O. & Manga, M. Two competing effects of volatiles on heat transfer in crystal-rich magmas: thermal insulation vs defrosting. *J. Petrol.* **51**, 847–867 (2010).
74. White, S. M., Crisp, J. A. & Spera, F. A. Long-term volumetric eruption rates and magma budgets. *Geochem. Geophys. Geosyst.* **7** (2006).
75. Rubin, A. M. Propagation of magma-filled cracks. *Annu Rev. Earth Planet. Sci.* **23**, 287–336 (1995).
76. Marsh, B. D. On the crystallinity, probability of occurrence, and rheology of lava and magma. *Contrib. Mineral. Petrol.* **78**, 85–98 (1981).
77. Lensky, N. G., Lyakhovsky, V. & Navon, O. Radial variations of melt viscosity around growing bubbles and gas overpressure in vesiculating magmas. *Earth Planet. Sci. Lett.* **186**, 1–6 (2001).